Composition, Structure, and Semiconducting Properties of MgxZr2-xN2 Thin Films

Sage R. Bauers*1, Danielle M. Hamann², Ashlea Patterson¹, John Perkins¹, Kevin R. Talley³,

Andriy Zakutayev*1

¹Materials Science Center, National Renewable Energy Laboratory, Golden, Colorado, 80401, United States

²Department of Chemistry and Materials Science Institute, University of Oregon, Eugene, Oregon, 97403, United States

³Department of Metallurgical and Materials Engineering, Colorado School of Mines, Golden, Colorado, 80401, United States

*E-mail: <u>sage.bauers@nrel.gov; andriy.zakutayev@nrel.gov</u>

Abstract

Synthesis and characterization of $Mg_xZr_{2-x}N_2$ (0.5 \leq x \leq 1.8) thin films deposited by reactive magnetron co-sputtering in nitrogen plasma is reported. Composition measurements show that nitrides with low oxygen content (less than 1%) can be formed up to x=1.0, at which point an increase in oxygen content is observed. Up to composition of x=1.6 the $Mg_xZr_{2-x}N_2$ thin films form in a rocksalt-derived crystal structure, as revealed by X-ray diffraction measurements. At x>1.6 the films rapidly oxidize. The lattice constant of the stoichiometric $MgZrN_2$ composition is a=4.537 Å, and only small changes in lattice parameter are observed with changing composition. Electrical conductivity decreases by several orders of magnitude with increasing Mg-content. The conductivity of Mg-rich (x \geq 1) films increases with increasing measurement temperature, indicating semiconducting character of Mg-rich $Mg_xZr_{2-x}N_2$. Optical absorption measurements of these Mg-rich samples show a clear absorption onset at 1.8 eV, also indicative of semiconducting behavior.

1. Introduction

Nitride semiconductors are attractive electronic materials due to their exceptional properties and chemical stability. These materials are typified by wurtzite-structured GaN and its alloys, which are by far the most studied nitride semiconductors.¹⁾ However, there are several other structural and chemical spaces where nitride semiconductors can be found.²⁾ For example, main-group metals also form nitride semiconductors in Π^{2+} -IV⁴⁺-N₂ derivatives of GaN (e.g. ZnGeN₂ and similar)^{3–5)} and in nitrogen-rich binary IV₃⁴⁺-N₄ spinel-like structures (e.g. Sn₃N₄)^{6,7)}. Many binary semiconductors containing transition metals are also known with a range of metal-nitrogen ratios (e.g. Cu₃N, Ta₃N₅, Zr₃N₄).^{8–10)} More recently ternary transition metal nitrides have been theoretically and experimentally studied in various structures, such as delafossites,¹¹⁾ perovskites,¹²⁾ wurtzites,¹³⁾ and several others.^{14,15)}

Despite these examples of nitride semiconductors outside of group-III mononitride family, most of the transition metal mononitrides are cubic refractory metals.¹⁶⁾ The few exceptions are ScN¹⁷⁾ and CrN¹⁸⁾, which are both narrow-gap semiconductors. These cubic transition metal mononitrides are particularly appealing for electronic applications since they can be epitaxially grown on substrates commonly used for other electronic materials, such as MgO, Al₂O₃, and Si.^{19–25)} Furthermore, (111) planes of transition metal mononitride rocksalts are also structurally compatible with (0001) GaN surfaces. For example, thin ScN buffer layers have been shown to improve the quality of electronics-grade GaN films²⁶⁾ and heteroepitaxy has been recently demonstrated between semiconducting GaN and superconducting NbN.²⁷⁾

Unfortunately, it remains challenging to grow high-quality ScN and CrN transition metal nitride semiconductors, and their sub-1 eV band gaps are too narrow for many uses. Recently, ternary rocksalt nitrides based on ScN, such as Al_xSc_{1-x}N or Mg_xSc_{1-x}N, or even superlattices made from these materials, have been explored since they allow for better control of charge transport properties. An alternative approach to design rocksalt nitride semiconductors is to alloy group-4 transition metal nitrides, such as TiN, with Mg. In this case, alloying with the electropositive Mg²⁺ moves the transition metal to a higher oxidation state until a semiconducting ternary compound, Mg*TM*N₂ (*TM*=Ti, Zr, Hf) is formed. Semiconducting behavior has been recently observed experimentally in MgTiN₂, MgZrN₂, and MgHfN₂, with slightly larger calculated band gaps in MgZrN₂ and MgHfN₂ than in MgTiN₂.

This paper focuses on the experimental synthesis and characterization of $Mg_xZr_{2-x}N_2$ (0.5 \leq x \leq 1.8) thin films, deposited by high-throughput combinatorial co-sputtering in nitrogen plasma. We show that these compounds are stabilized in a rocksalt-derived structure over a large range of chemical compositions. Mg-poor films (x \leq 1) are nearly oxygen-free, but oxygen begins replacing nitrogen at Mg-rich compositions (x \geq 1). At compositions of about x=1.6 the maximum Mg-solubility is reached, the rocksalt-derived structure is lost, and oxygen fully replaces nitrogen in the films. As x increases in $Mg_xZr_{2-x}N_2$, the conductivity decreases by several orders of magnitude and an optical absorption onset emerges in the visible spectral range. Furthermore, temperature-dependent conductivity measurements at Mg-rich compositions show thermally activated conduction, also indicative of semiconducting transport behavior.

2. Materials and methods

2.1 Methods

Figure 1 schematically presents the combinatorial approach used for the deposition of Mg_xZr₂. xN₂ thin films. These films were synthesized via radio frequency (RF) reactive co-sputtering from 2" diameter Mg (99.98+% purity) and Zr (99.9+% purity) metallic targets held between 20-40 W and 40-60 W respectively. The deposition atmosphere was held at 5 mTorr pressure composed of equal amounts of nitrogen and of argon (99.999+% purity each), achieved by flowing 6 sccm of each gas through the deposition chamber and evacuating with a throttled turbomolecular pump.^{37,38)} Unless otherwise noted, as the nitrogen gas was introduced into the chamber it passed through an RF coil at 350 W power, which raised the nitrogen activity by breaking the N₂ molecule. The substrates were heated to temperatures between 240-570 °C, which were determined beforehand using a thermocouple bonded to the substrate surface and measured without plasma present.

As shown in Figure 1, the two sputter cathodes were 180° opposed with respect to the vertical axis of the chamber, and obliquely oriented at a 50° angle with respect to the plane of the stationary glass or Si substrates. The activated nitrogen source was positioned at normal incidence to the central position of the substrates. This geometry resulted in thin films with a 1-dimensional gradient in composition. While the composition gradients are continuous, to facilitate characterization each substrate was deposited through a shadow mask and discretized,

with 11 compositionally-distinct columns and 4 compositionally-redundant rows. The deposition geometry shown in Figure 1 creates a gap between the two substrates, which spatially corresponds to about one missing point. Thus, substrate A (Mg-rich) contains columns 1-11, and substrate B (Zr-rich) contains columns 13-23, with column 12 left out due to the gap. Alternatively, a single centered substrate may also be used, containing columns 7-17 of the two-substrate geometry. Whether a single or double substrate configuration is used, each deposited specimen is referred to as a combinatorial "sample library."

The thin film sample libraries in this study were characterized for structure using x-ray diffraction (XRD), thickness using stylus profilometry, composition using electron probe microanalysis (EPMA) and Rutherford backscattering (RBS), transmittance and reflectance spectra using ultraviolet-visible range optical spectroscopy (UV-Vis), and sheet resistance using four-point probe measurements, with previously described instruments.^{39–42)} Each of these spatially-resolved measurements was set up to probe the same 44 digitized positions of the sample libraries. For composition measurements using EPMA, extra steps were taken for quantitative analysis of light elements. Different beam energies are used to fluoresce the sample at different depths, and k-ratios are determined at each. These k-ratios are used to iteratively solve for the film's thickness-density as a function of beam energy until a self-consistent composition is obtained for each element.³⁹⁾ At most points, analytical total compositions sum to slightly less than 1, possibly due to impurities from sputter targets.

Structure and property measurements were carried out at every point on the samples, and only small changes were observed along the redundant rows orthogonal to the composition gradients. The center rows were used for values reported in this manuscript. Unless otherwise noted, composition measurements were carried out on odd columns of the sample and interpolation was used to infer composition of the unmeasured points. The data were processed using a custom written package in the Igor Pro environment, which facilitates organization, visualization, and analysis of combinatorial materials science data sets. Data resulting from these experiments will be made available through High Throughput Experimental Materials Database (HTEM DB) at https://htem.nrel.gov/. (43)

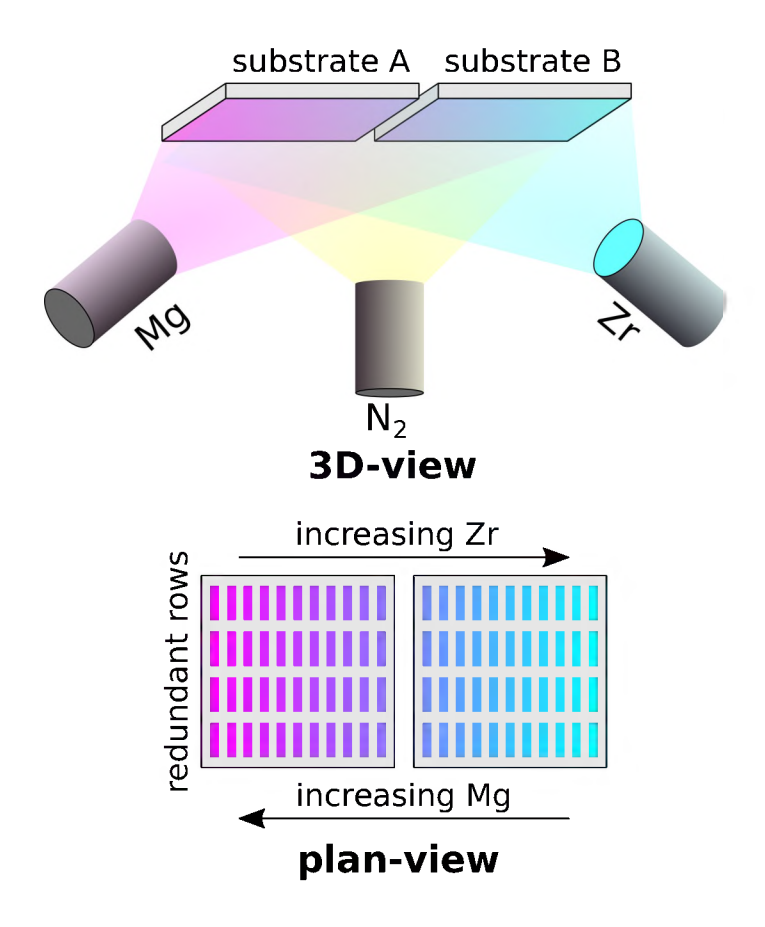


Figure 1: Schematic of the combinatorial thin-film synthesis approach used for the formation of Mg_xZr_{2-x}N₂ sample libraries. A single centered substrate was also used as an alternative to the two-substrate geometry shown here.

2.2 Materials

To assess the chemical stability range of Mg_xZr_{2-x}N_{2-y}O_y thin films, two sets of combinatorial sample libraries were prepared on bare Si substrates for composition measurements via electron probe microanalysis (EPMA). In this chemical formula, x and y express the measured Mg/cation and O/anion fractions respectively, and assumes the total number of cations and anions is identical, as for an ideal rocksalt structure.

The first set of sample libraries was prepared in a double-substrate configuration to assess stability over a broad range of metal compositions. Odd columns were measured along row 2, resulting in 12 distinct measurements evenly spread across the compositionally graded

dimension. In order to minimize oxygen contamination, these sample libraries were prepared in activated nitrogen and surrounded by a cryogenic sheath. Prior to deposition the chamber was baked at 100 °C for 3 days, and partial pressures of oxygen-containing species (H₂O, O₂, OH) were all measured with a residual gas analyzer to be below 10⁻⁸ torr. Immediately after preparation, the sample libraries were vacuum-sealed into a plastic bag, and stored in an inert N₂ environment prior to composition measurements. We refer to this sample library as *oxygen-free*.

Another sample library was prepared in the single-substrate configuration and without chamber bake-out or activated nitrogen, and allowed to passively oxidize in ambient conditions before measurement. This *oxygen-containing* thin film sample library was similarly analyzed with EPMA, but all columns were measured. In order to verify that columns were parallel to the composition gradient, some measurements were made along the redundant rows of the sample library, which showed less than 2% variation in atomic percentages.

We also prepared several additional thin film sample libraries with conditions similar to the oxygen-free library described above. However, these sample libraries were made on glass substrates for structure and properties measurements, and were allowed post-deposition oxygen exposure. Compositions of these sample libraries were determined by RBS as opposed to EPMA. Detailed anion composition experiments were not carried out on these sample libraries, so we refer to them with the general chemical formula Mg_xZr_{2-x}N₂. All of these thin film samples had thicknesses in 100-350 nm range.

3. Results and discussion

3.1 Chemical composition

Figure 2a presents composition of the oxygen-free sample library as a function of column number along the 1D combinatorial gradient, normalized to the total composition. The upper-right axis is the analytical total from EPMA. At Zr-rich compositions the films are almost pure nitrides, with <1 at% oxygen. Moving from right-to-left in Figure 2a the oxygen content increases from about 0% to 50% while the total anion fraction decreases. Column 11 is the first point with >1 at% oxygen, which corresponds to x=1.53 cation composition. After column 9, which corresponds to Mg_{1.63}Zr_{0.37}N_{1.45}O_{0.06}, the oxygen content rapidly increases. By column 5 practically no nitrogen is measured. This suggests an upper limit for Mg that can be incorporated

into $Mg_xZr_{2-x}N_2$ thin films of about 0.8 cation fraction (x \approx 1.6) before the material is no longer air-stable.

Composition data from both the oxygen-free and oxygen-containing sample libraries are presented in **Figure 2b** as a ternary phase diagram. Like the oxygen-free sample, an increase in oxygen content with increasing Mg concentration is also observed in the oxygen-containing sample. However, there is a higher oxygen content at each cation composition as expected from the preparation and storage, and the increase is less steep than the rapid increase observed in oxygen-free films. Specifically, the oxygen ranges from ca. 3-7 at% over the same cation stoichiometry where the oxygen free sample is still under 1 at% oxygen.

As seen in Figure 2b, the oxygen-free samples show slightly sub-stoichiometric anion content. This could partially be due to imperfect EPMA k-ratio models, which total to slightly less than unity (>0.95), or due to large a number of nitrogen vacancies. However, since the oxygen-containing sample shows slightly higher total anion content, perhaps oxygen compensates nitrogen sub-stoichiometry, either during growth or post-deposition, but without further nitrogen effusion from the material. Figure 2b shows that for $0 \le x \le 1$ in $Mg_xZr_{2-x}N_2$, the measured compositions are on the $ZrN \rightarrow MgZrN_2$ tie-line and for x > 1, the $MgZrN_2 \rightarrow Mg_3N_2$ tie-line is roughly followed before the sample becomes fully oxidized, at which point the anion content increases and MgO is formed.

Since oxygen content changes as a function of metal composition, it is interesting to consider the stabilization mechanisms in $Mg_xZr_{1-x}N_{1-y}O_y$ thin films. While not strictly ionic, ⁴⁴⁾ we consider ZrN as charge-balanced Zr³⁺ cations and N³⁻ anions. When Mg^{2+} is added to the structure, a higher Zr^{4+} oxidation state is expected due to the inductive effect, ⁴⁵⁾ forming $Mg^{2+}Zr^{4+}N_2^{3-}$. Thus, for $x\le 1$, the compound could be stabilized via partial change in the valence of Zr atoms from Zr^{3+} to Zr^{4+} . A similar effect was recently observed in different compositions of Zn_xMoN_y for Mo^{4+} and Mo^{6+} oxidation states of $Mo.^{13)}$ For Mg-contents greater than x=1, this redox effect cannot stabilize the excess 2+ cation, since Zr is already in its highest oxidation state. It was previously shown by density functional theory that $Mg_xTi_{2-x}N_2$ is thermodynamically unstable at x>1, and that sub-stoichiometric nitrogen contents are energetically favorable at these compositions.³⁵⁾ This is in agreement with our data from the

oxygen-free library. However, since the oxygen-containing library also has larger anion fractions, we speculate that instead of maintaining a reduced anion content, it becomes favorable to form an oxynitride by 1:1 substitution of N^{3-} for O^{2-} on the anion sublattice, which compensates the excess charge.

To summarize this behavior, both charge balance and 1:1 cation/anion ratios are maintained for all x per the following formulas:

$$Mg_xZr_{2-x}N_2$$
 for $0 \le x \le 1$ (redox balanced). (1)

$$Mg_xZr_{2-x}N_{4-2x}O_{2x-2}$$
 for $1 \le x \le 2$ (oxygen balanced). (2)

Figure 2c shows the calculated oxygen anion fraction as a function of the magnesium cation fraction for these charge-balanced chemical formulae, overlaid with the measured composition from both oxygen-free and -containing samples. The oxygen-free composition follows the calculated line below x=1, but does not follow this line at higher Mg composition, likely due to the oxygen-starved deposition and storage environments. The $Mg_xZr_{2-x}N_2$ rocksalt-like phase width, discussed in further detail in the following section, extends well past the predicted $x\le 1$ thermodynamic stability window for $Mg_xTi_{2-x}N_2$, 35) perhaps due to kinetic limitations of the sputtering process. Data from the oxygen-containing sample have similar shape to the charge-balanced curve in Figure 2c, but lag slightly in oxygen content. It is possible this lags the charge-balanced model due to the aforementioned kinetic effects of sputtering. Verifying these proposed stabilization mechanisms with deliberate formation of oxynitride quaternaries would be an interesting follow-up study.

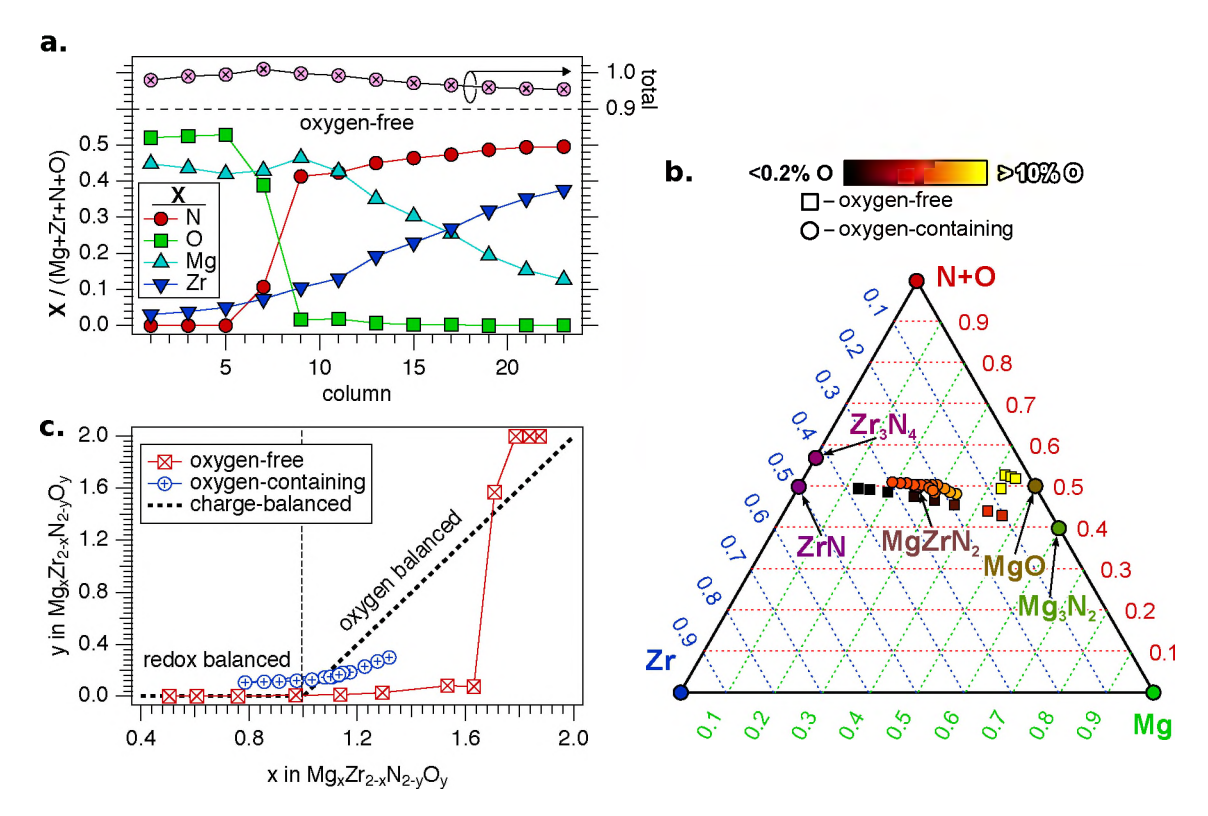


Figure 2: Composition of Mg_xZr_{2-x}N_{4-2x}O_{2x-2} thin films. (a) Compositions measured from the oxygen-free sample library, which shows rapid oxidation at Mg-rich compositions. (b) Ternary plot showing all samples measured by EPMA with a combined anion axis. (c) oxygen anion fraction as a function of magnesium cation fraction, plotted against a charge-balanced ionic model with equal number of cations and anions, as expected for rocksalt structure.

3.2 Crystal structure

X-ray diffraction data from $Mg_xZr_{2-x}N_2$ sample libraries are shown in Figure 3. Diffractograms for various $Mg_xZr_{2-x}N_2$ compositions grown at 525 °C (**Figure 3a**) exhibit peaks that can be indexed to a rocksalt structure (space group 225), in agreement with our previous experiments and calculations on $MgZrN_2$. However, since $Mg_xZr_{2-x}N_2$ contains 2 instead of 1 cations, we refer to this crystal structure as "rocksalt-derived" throughout the text. There is negligible structural change over a broad composition range $(0.5 \le x \le 1.3)$, but there are changes in the crystalline texture of the thin films. At high Zr composition fractions the films exhibit (100) texture, and gradually shift to being more polycrystalline with increasing Mg content, as seen by emergent (111) and (220) peaks.

The d-spacing of the (002) peak, corresponding to one-half of the a-lattice parameter, is shown above the diffractograms in Figure 3a, and decreases only slightly with increasing Mg. This structural tolerance and very small shift in lattice parameter is likely due to 6-coordinate Mg²⁺ and Zr⁴⁺ having practically identical Shannon radii of 0.72Å. ⁴⁶⁾ Binary ZrN rocksalt has a lattice parameter of 4.585(2) Å. ⁴⁷⁾ We see reasonable agreement of $a \approx 4.55$ Å when extrapolating the d-spacing of the (002) peak in Mg_xZr_{2-x}N₂ films to x=0.

Figure 3b shows a heatmap of diffracted intensity as a function of composition and diffraction angle for 22 points in a sample library. The peaks from the rocksalt-derived structure persist until a composition of ca. Mg_{1.6}Zr_{0.4}N₂, at which point a broad low intensity reflection is observed. This correlates well with the composition at which the samples become highly oxidized, so this reflection may be associated with amorphous/nanocrystalline MgO. A line scan showing this low intensity reflection is also presented for the Mg_{1.67}Zr_{0.33}N₂ composition in Figure 3a. Taken together, the composition and diffraction data suggest an effective Mg solubility limit of about 0.8 cation fraction in rocksalt-derived Mg_xZr_{2-x}N₂. However higher Mg fractions possibly could be observed with encapsulation of the films to protect from excess oxidation.

Crystallite texture also changes as a function of deposition temperature in Mg_xZr_{2-x}N₂ thin films. **Figure 3c** presents a color map showing texture of Mg_xZr_{2-x}N₂ as a function of deposition temperature and composition. Texture is expressed here as the fraction of (111) peak area. Figure 3c is split into three regions showing trends corresponding to weak, medium, and strong crystallinity. Since the X-ray scattering power changes with composition x in Mg_xZr_{2-x}N₂, the combined areas of the diffraction peaks were first normalized to the metal ratios (and film thickness) before defining these regions. However, these regions still only indicate general trends rather than a quantitative evaluation of crystal quality. At deposition temperatures greater than about 400 °C, where the strongest crystallinity is observed, crystallinity decreases with increasing Mg-content. The opposite trend is seen at lower temperatures.

For most conditions, crystallites are preferentially oriented in (111) texture, with strong (100) texture only present from Zr-rich compositions deposited at high temperatures (Figure 3c). On the other hand, low temperature growth results in more polycrystalline material. Based on

demonstrations of epitaxial ScN growth on (100)- and (111)-oriented MgO and Si substrates^{19,24,25)} and its similar lattice parameter to MgZrN₂, it is reasonable that similar epitaxial compatibility will be possible. Since both (100) and (111) textured thin films are observed under different growth conditions on amorphous substrates, perhaps the propensity to adopt these orientations can be used to promote epitaxial growth on different substrates. For example, growth of stoichiometric MgZrN₂ on (111) MgO or (0001) GaN at intermediate temperatures could form higher quality films since there is already more (111) texture on amorphous substrates. On the other hand, higher temperatures or higher Zr-content might be required for epitaxial growth on (100) MgO.

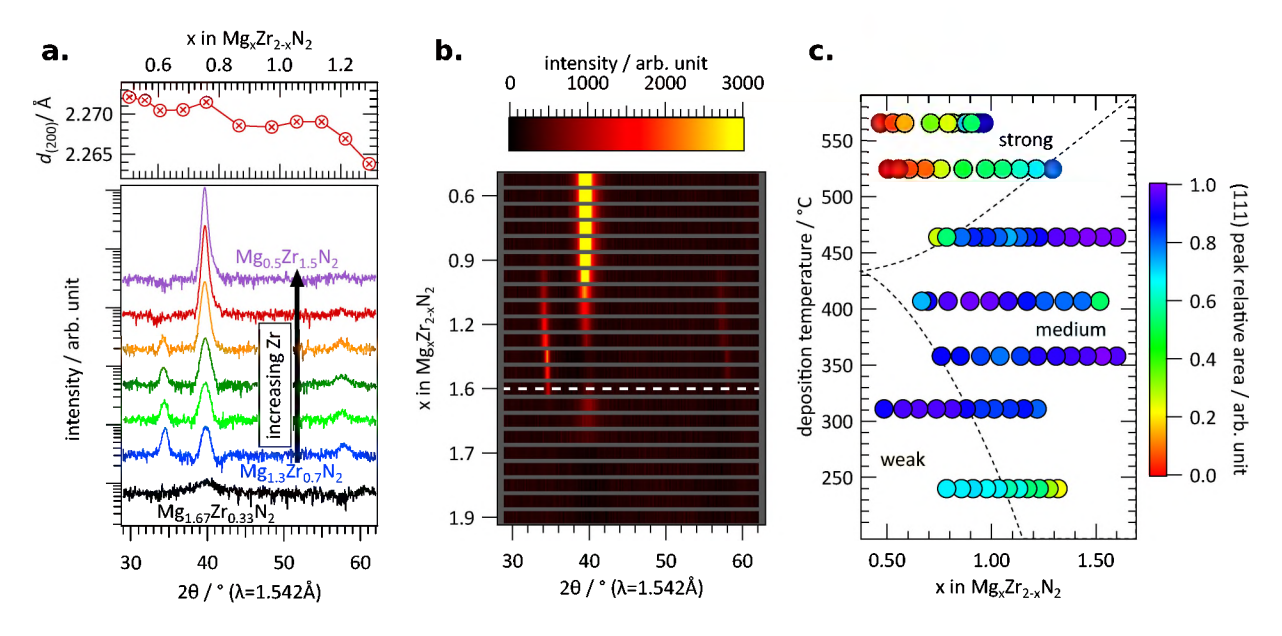


Figure 3: X-ray diffraction from $Mg_xZr_{2-x}N_2$ thin films. (a) Diffraction patterns and d-spacing of (200) rocksalt peak for selected compositions in a combinatorial sample library. (b) Heatmap of diffracted intensity as a function of composition and diffraction angle. The rocksalt-like structure is lost above $x \approx 1.6$, indicated by a horizontal dashed line. (c) Intensity fraction of (111) reflection as a function of deposition temperature and composition. The plot is split into regions of weak, medium, and strong crystallinity.

3.3 Electrical and optical properties

Electrical conductivity data collected from $Mg_xZr_{2-x}N_2$ thin films are shown in Figure 4. As seen in **Figure 4a**, the room-temperature conductivity is relatively insensitive to deposition temperature, fluctuating only slightly and non-monotonically. On the other hand, the

conductivity changes by 6 orders of magnitude within the studied composition range of the films. At stoichiometric MgZrN₂ compositions, the films have intermediate conductivity (\approx 1-100 S cm⁻¹). Assuming mobilities on the order of 0.1 cm² V⁻¹s⁻¹, typical of polycrystalline sputtered nitride thin films on glass, we infer a carrier density of about 10^{21} cm⁻³. The samples become more metallic (>100 S cm⁻¹) when made Zr-rich, and more insulating when made Mg-rich (<1 S cm⁻¹). These Mg-rich samples had resistances near the upper-limit of the measurement equipment (ca. $10^7 \Omega$).

Based on our redox/composition charge-balance model (Eq. 1-2), Zr compositions greater than MgZrN₂ will lead to a partially filled Zr *d*-shell, and would be expected to exhibit metallic behavior. On the other hand, stoichiometric MgZrN₂ should be semiconducting with finite carrier density. Excess Mg possibly compensates for donor defects, reducing the free carrier density and conductivity, an effect observed in similar wurtzite structured ternary nitrides.⁵⁾ Thus, the composition-dependent changes in conductivity observed here are quite reasonable.

Figure 4b shows temperature-dependent conductivity measurements from a $Mg_xZr_{2-x}N_2$ thin film grown at 410 °C, normalized to the measurement at 30 °C. The reduced composition range relative to Figure 4a is due to data similarity (σ/σ_{30} °C ≈ 1.0 for all T_{meas}) on the Zr-rich side, and noise levels greater than $\Delta\sigma$ on the Mg-rich side (due to being at the upper resistance limit). For Zr-rich compositions, no change in conductivity is observed, despite this being significantly below the Debye temperature for ZrN. On the other hand, a gentle increase in conductivity with increasing temperature is observed in stoichiometric and Mg-rich compositions. Such an increase in conductivity is typically associated with thermal activation of additional free charge carriers, further corroborating the semiconducting nature of these compositions.

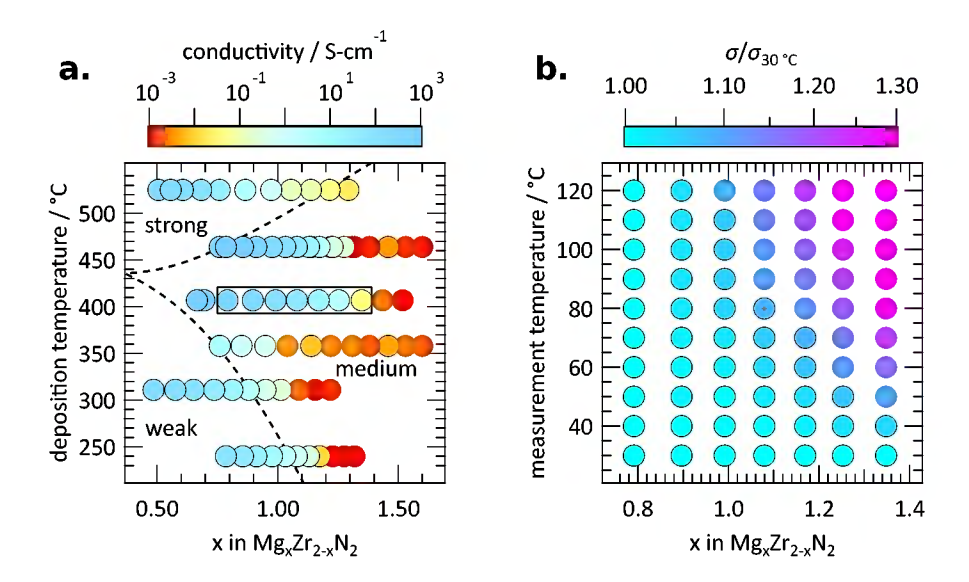


Figure 4: Electrical conductivity of Mg_xZr_{2-x}N₂ thin films. (a) Color map of conductivity as a function of the deposition temperature and chemical composition. The three regions of weak, medium, and strong crystallinity are described in the main text. (b) Temperature-dependent conductivity measured from the 410 °C deposition temperature points highlighted by a black box in Figure 4a.

UV-Vis optical spectroscopy data were also collected from Mg_xZr_{2-x}N₂ thin films grown at 460 °C, and the resulting absorption spectra are presented in Figure 5. **Figure 5a** shows absorption curves for two compositions: Mg_{0.97}Zr_{1.03}N₂, which is close to stoichiometric MgZrN₂, and Mg_{1.53}Zr_{0.47}N₂, which is approaching the upper Mg limit before the rocksalt-derived structure is lost. As seen in the Mg_{0.97}Zr_{1.03}N₂ spectrum, a high absorption coefficient of ca. 10⁵ cm⁻¹ is observed across the entire measured energy range. The shape and magnitude of the absorption curve is similar to Mg_xTi_{1-x}N₂ films with similar composition, but with the absorption minimum shifted from 1.7 to 2.2 eV.³²⁾ This energy is higher than the calculated electronic bandgap of MgZrN₂ with an ordered cation sub-lattice, which has a dipole-forbidden optical transition.³⁴⁾ Furthermore, a Burnstein-Moss shift might be present in experimental samples, since the larger absorption strength at low energy suggests absorption from free-carriers. These results warrant further exploration of the optical properties of Zr-rich Mg_xZr_{1-x}N₂ as a potential infrared plasmonic material, similar to MgTiN₂⁴⁸⁾

For the Mg-rich Mg_{1.53}Zr_{0.47}N₂ composition, the sub-gap absorption is much lower, suggesting that free carriers are compensated at Mg-rich compositions. The primary absorption onset for this composition occurs at about 1.8 eV. This value is lower than the 2.2 eV absorption minima for the Mg_{0.97}Zr_{1.03}N₂ composition, but the absorption spectrum is generally shifted to higher energy. **Figure 5b** shows a heatmap of absorption coefficient across a combinatorial library as a function of photon energy and chemical composition. At compositions with Mg content lower than MgZrN₂, almost no absorption onset is observed, and above this a gentle shift in the absorption onset of about 0.4 eV is seen. The shift in absorption edge and dramatic change in sub-gap absorption suggest that both electronic and optical properties can be tuned with metal composition in Mg_xZr_{2-x}N₂ thin films. However, since different defects were recently theoretically suggested to allow for bipolar doping in stoichiometric MgTiN₂, ³⁶⁾ and both cation ordering⁴⁹⁾ and the presence of oxygen⁵⁰⁾ are known to significantly affect the properties of other heterovalent ternary nitrides, additional work must be done to better understand the optical and electrical properties of these off-stoichiometric Mg_xZr_{2-x}N₂ compositions.

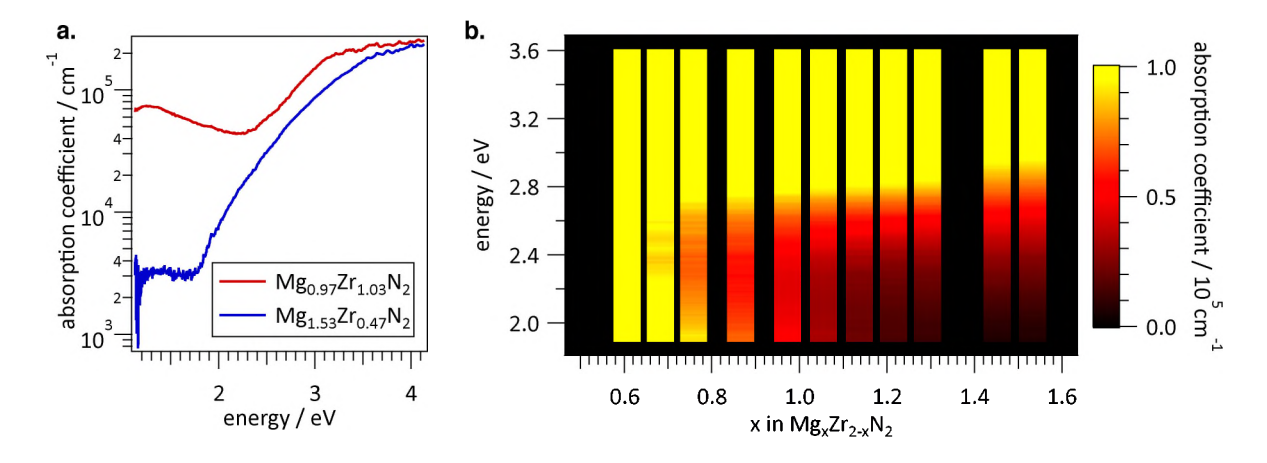


Figure 5: Optical absorption spectra of $Mg_xZr_{2-x}N_2$ thin films. (a) Spectra of stoichiometric and Mg-rich compositions. (b) Spectra from compositions across a $Mg_xZr_{2-x}N_2$ combinatorial library.

4. Conclusions

We have reported on the growth, stability, optical and electrical properties of Mg_xZr_{2-x}N₂ thin films (0.5≤x≤1.8). The films were deposited on glass and Si substrates via combinatorial magnetron co-sputtering from metallic targets in the presence of nitrogen plasma. Slightly substoichiometric nitrogen concentrations were measured, especially at Mg-rich compositions. X-ray diffraction measurements show that the nitride thin-films crystallize in a rocksalt-derived

structure over a broad composition range, and that crystallinity and crystallite orientation change with both the composition and deposition temperature. At Mg compositions greater than about Mg_{1.6}Zr_{0.4}N₂, the rocksalt-derived structure is lost and replacement of nitrogen for oxygen is observed. A semiconducting character of Mg-rich compositions is evident, observed in both temperature-activated conductivity and clear onset in the optical absorption spectrum. Taken as a whole, our experiments highlight Mg_xZr_{2-x}N₂ as a new chemical space for semiconducting nitrides. While the rocksalt-derived structure is quite stable, the microstructure, anion composition, and properties of these new materials change both with the metal composition and growth conditions, prompting further investigation in optimizing synthesis of these novel materials.

Acknowledgements

This work was authored by the National Renewable Energy Laboratory, operated by Alliance for Sustainable Energy, LLC, for the U.S. Department of Energy (DOE) under Contract No. DE-AC36-08GO28308. The funding was provided by Office of Science (SC), Office of Basic Energy Sciences (BES), as part of the Energy Frontier Research Center "Center for Next Generation of Materials Design: Incorporating Metastability." D.H.M. was supported by the National Science Foundation Graduate Research Fellowship Program under Grant No. 1309047. A.P. acknowledges support by the U.S. Department of Energy, Office of Science, Office of Workforce Development for Teachers and Scientists (WDTS) under the Science Undergraduate Laboratory Internship (SULI) program. Author K.R.T. was supported by the US National Science Foundation (DMREF-1534503). The authors would like to thank John Donovan at the Center for Advanced Materials Characterization in Oregon (CAMCOR) analytical facility for technical assistance during electron microprobe data collection. The views expressed in the article do not necessarily represent the views of the DOE or the U.S. Government.

References

- 1) F. Ponce, and D. P. Bour, Nature **386**, 351 (1997).
- 2) A. Zakutayev, J. Mater. Chem. A 4, 6742 (2016).
- 3) W. L. Larson, H. P. Maruska, and D. A. Stevenson, J. Electrochem. Soc. **121**, 1673 (1974).

- 4) A. Punya, W. R. L. Lambrecht, and M. Van Schilfgaarde, Phys. Rev. B **84**, 165204 (2011).
- 5) A. N. Fioretti, A. Zakutayev, H. Moutinho, C. Melamed, J. D. Perkins, A. G. Norman, M. Al-Jassim, E. S. Toberer, and A. C. Tamboli, J. Mater. Chem. C 3, 11017 (2015).
- 6) T. D. Boyko, A. Hunt, A. Zerr, and A. Moewes, Phys. Rev. Lett. 111, (2013).
- 7) C. M. Caskey, J. A. Seabold, V. Stevanović, M. Ma, W. A. Smith, D. S. Ginley, N. R. Neale, R. M. Richards, S. Lany, and A. Zakutayev, J. Mater. Chem. C 3, 1389 (2015).
- 8) W. J. Chun, A. Ishikawa, H. Fujisawa, T. Takata, J. N. Kondo, M. Hara, M. Kawai, Y. Matsumoto, and K. Domen, J. Phys. Chem. B **107**, 1798 (2003).
- 9) A. Zerr, G. Miehe, and R. Riedel, Nat. Mater. 2, 185 (2003).
- 10) C. M. Caskey, R. M. Richards, D. S. Ginley, and A. Zakutayev, Mater. Horiz. 1, 424 (2014).
- 11) A. Zakutayev, A. J. Allen, X. Zhang, J. Vidal, Z. Cui, S. Lany, M. Yang, F. J. Disalvo, and D. S. Ginley, Chem. Mater. 26, 4970 (2014).
- 12) R. Sarmiento-Pérez, T. F. T. Cerqueira, S. Körbel, S. Botti, and M. A. L. Marques, Chem. Mater. 27, 5957 (2015).
- E. Arca, S. Lany, J. D. Perkins, C. Bartel, J. Mangum, W. Sun, A. Holder, G. Ceder, B. Gorman, G. Teeter, W. Tumas, and A. Zakutayev, J. Am. Chem. Soc. **140**, 4293 (2018).
- 14) Y. Hinuma, T. Hatakeyama, Y. Kumagai, L. A. Burton, H. Sato, Y. Muraba, S. Iimura, H. Hiramatsu, I. Tanaka, H. Hosono, and F. Oba, Nat. Commun. 7, 11962 (2016).
- W. Sun, C. Bartel, E. Arca, S. Bauers, B. Matthews, B. Orvañanos, B.-R. Chen, M. F. Toney, L. T. Schelhas, W. Tumas, J. Tate, A. Zakutayev, S. Lany, A. Holder, and G. Ceder, arXiv:1809.09202
- 16) H. Holleck, J. Vac. Sci. Technol. A Vacuum, Surfaces, Film. 4, 2661 (1986).
- 17) W. R. L. Lambrecht, Phys. Rev. B 62, 13538 (2000).
- 18) A. Herwadkar, and W. R. L. Lambrecht, Phys. Rev. B 79, (2009).
- 19) S. Kerdsongpanya, N. Van Nong, N. Pryds, A. Žukauskaitė, J. Jensen, J. Birch, J. Lu, L. Hultman, G. Wingqvist, and P. Eklund, Appl. Phys. Lett. **99**, 232113 (2011).
- 20) C. X. Quintela, J. P. Podkaminer, M. N. Luckyanova, T. R. Paudel, E. L. Thies, D. A. Hillsberry, D. A. Tenne, E. Y. Tsymbal, G. Chen, C.-B. Eom, and F. Rivadulla, Adv. Mater. 27, 3032 (2015).
- 21) K. Inumaru, K. Koyama, N. Imo-Oka, and S. Yamanaka, Phys. Rev. B 75, (2007).

- 22) R. Li, J. S. Gandhi, R. Pillai, R. Forrest, D. Starikov, and A. Bensaoula, J. Cryst. Growth 404, 1 (2014).
- J. Narayan, P. Tiwari, X. Chen, J. Singh, R. Chowdhury, and T. Zheleva, Appl. Phys. Lett. 61, 1290 (1992).
- 24) M. A. Moram, S. V. Novikov, A. J. Kent, C. Nörenberg, C. T. Foxon, and C. J. Humphreys, J. Cryst. Growth 310, 2746 (2008).
- M. A. Moram, Z. H. Barber, C. J. Humphreys, T. B. Joyce, and P. R. Chalker, J. Appl. Phys. 100, 023514 (2006).
- 26) M. A. Moram, Y. Zhang, M. J. Kappers, Z. H. Barber, and C. J. Humphreys, Appl. Phys. Lett. 91, 152101 (2007).
- 27) R. Yan, G. Khalsa, S. Vishwanath, Y. Han, J. Wright, S. Rouvimov, D. Scott Katzer, N. Nepal, B. P. Downey, D. Muller, huili G. Xing, D. J. Meyer, and D. Jena, Nature 555, 183 (2018).
- 28) B. Saha, S. Saber, G. V. Naik, A. Boltasseva, E. A. Stach, E. P. Kvam, and T. D. Sands, Phys. status solidi **252**, 251 (2015).
- 29) B. Saha, M. Garbrecht, J. A. Perez-Taborda, M. H. Fawey, Y. R. Koh, A. Shakouri, M. Martin-Gonzalez, L. Hultman, and T. D. Sands, Appl. Phys. Lett. **110**, 252104 (2017).
- 30) B. Saha, A. Shakouri, and T. D. Sands, Cit. Appl. Phys. Rev. 5, (2018).
- 31) M. Fenker, M. Balzer, H. Kappl, and O. Banakh, Surf. Coatings Technol. 200, 227 (2005).
- 32) B. Wang, S. Kerdsongpanya, M. E. McGahay, E. Milosevic, P. Patsalas, and D. Gall, J. Vac. Sci. Technol. A **36**, 061501 (2018).
- 33) M. A. Gharavi, R. Armiento, B. Alling, and P. Eklund, J. Mater. Sci. 53, 4294 (2018).
- 34) S. R. Bauers, A. Holder, W. Sun, C. L. Melamed, R. Woods-Robinson, J. Mangum, J. Perkins, W. Tumas, B. Gorman, A. Tamboli, G. Ceder, S. Lany, and A. Zakutayev, arXiv:1810.05668
- 35) B. Alling, Phys. Rev. B **89**, 085112 (2014).
- 36) Y. Irokawa, and M. Usami, Jpn. J. Appl. Phys. 55, 098001 (2016).
- A. Bikowski, S. Siol, J. Gu, A. Holder, J. S. Mangum, B. Gorman, W. Tumas, S. Lany, and A. Zakutayev, Chem. Mater. **29**, 6511 (2017).
- 38) K. R. Talley, S. L. Millican, J. Mangum, S. Siol, C. B. Musgrave, B. Gorman, A. M. Holder, A. Zakutayev, and G. L. Brennecka, Phys. Rev. Mater. **2**, 063802 (2018).
- 39) T. M. Phung, J. M. Jensen, D. C. Johnson, J. J. Donovan, and B. G. McBurnett, X-Ray

- Spectrom. 37, 608 (2008).
- 40) L. R. Doolittle, Nucl. Instruments Methods Phys. Res. Sect. B Beam Interact. with Mater. Atoms 15, 227 (1986).
- 41) A. Zakutayev, T. R. Paudel, P. F. Ndione, J. D. Perkins, S. Lany, A. Zunger, and D. S. Ginley, Phys. Rev. B 85, 085204 (2012).
- A. Zakutayev, F. J. Luciano, V. P. Bollinger, A. K. Sigdel, P. F. Ndione, J. D. Perkins, J. J. Berry, P. A. Parilla, and D. S. Ginley, Rev. Sci. Instrum. 84, 053905 (2013).
- 43) A. Zakutayev, N. Wunder, M. Schwarting, J. D. Perkins, R. White, K. Munch, W. Tumas, and C. Phillips, Sci. Data 5, 180053 (2018).
- 44) K. Schwarz, Crit. Rev. Solid State Mater. Sci. 13, 211 (1987).
- 45) J. Etourneau, J. Portier, and F. Ménil, J. Alloys Compd. 188, 1 (1992).
- 46) R. D. Shannon, and IUCr, Acta Crystallogr. Sect. A 32, 751 (1976).
- 47) A. N. Christensen, V. Romano, R. Hesse, A. F. Andresen, and P. Fischer, Acta Chem. Scand. **29a**, 563 (1975).
- 48) C. Metaxa, S. Kassavetis, J. F. Pierson, D. Gall, and P. Patsalas, ACS Appl. Mater. Interfaces 9, 10825 (2017).
- 49) S. Lany, A. N. Fioretti, P. P. Zawadzki, L. T. Schelhas, E. S. Toberer, A. Zakutayev, and A. C. Tamboli, Phys. Rev. Mater. 1, 035401 (2017).
- 50) J. Pan, J. Cordell, G. J. Tucker, A. Zakutayev, A. C. Tamboli, and S. Lany, Adv. Mater. 1807406 (2019). doi:10.1002/adma.201807406